Journal of the Physical Society of Japan **89**, 044002 (2020)
https://doi.org/10.7566/JPSJ.89.044002

Stationary-state Electron Scattering Using a Complex Injecting Potential

Tomokazu Yamaguchi[1], Kazuki Uchida[1], Kálmán Varga[2], and Kazuyuki Watanabe[1]*

[1]*Department of Physics, Tokyo University of Science, Shinjuku, Tokyo 162-8601, Japan*
[2]*Department of Physics and Astronomy, Vanderbilt University, Tennessee 37235, U.S.A.*

(Received November 18, 2019; accepted February 10, 2020; published online March 9, 2020)

We simulated stationary electron scattering by solving the time-dependent Schrödinger equation with a complex injecting potential (CIP). The calculated electron transmission probabilities through one-dimensional potentials and the electron interference patterns caused by double slits show good agreement with analytical results. The Aharonov–Bohm effect is also clearly demonstrated by the presence of a vector potential at one side of the double-slit configuration. The stationary electron-scattering method by a CIP can be straightforwardly extended to studies of various electron-emission phenomena as well as electron-transport phenomena in the framework of time-dependent density functional theory.

1. Introduction

Electron scattering is the one of the most fundamental phenomena in quantum physics and has been applied to many experimental techniques, such as transmission electron microscopy (TEM), scanning electron microscopy (SEM), and electron holography. Stationary-state electron scattering is observed in electron scattering experiments for long-time-period electron beam injection. Theoretical investigations of electron scattering are often performed using the Lippmann–Schwinger (LS) equation with the Born approximation. However, electron scattering by realistic systems, such as at surfaces and molecules, are often beyond the regime of the Born approximation. Therefore, it is necessary to directly solve the time-dependent Schrödinger equation (TDSE) for a complete understanding of the electron scattering processes.

In previous studies, the wave packet (WP) electron scattering method was used for solving the TDSE[1)] and the time-dependent density functional theory (TDDFT). Using the latter method, secondary electron emission (SEE),[2,3)] angle-resolved secondary electron emission (ARSEE),[4)] electron transmittance,[5)] low-energy electron diffraction (LEED),[6,7)] and the electron Talbot effect on graphene[8)] have been investigated. In the WP simulation in Ref. 6, the transmission coefficients were calculated by extracting the plane wave components from the Fourier transformed transmitted wave. Short-time-period (transient) electron scattering can be investigated using this method, but long-time-period (stationary) electron scattering, which is realized in experiments, cannot be investigated.

In 2012 a method that enables simulation of stationary-state electron scattering was developed by Wibking and Varga, called the *complex injecting potential* (CIP) method.[9)] The advantage of the CIP over previous studies is that the desired state can be injected into the system and the stationary state can be reached. Figure 1 shows a wave function scattered by a square well potential in the WP propagating method [Fig. 1(a)] and CIP method [Fig. 1(b)]. Using the CIP method, He et al. simulated stationary-state electron transport and investigated local currents in graphene nanoribbons and other materials.[10)] In the present study, we simulate stationary-state electron scattering in one dimension and in a double-slit system using the CIP to check the validity and accuracy of the CIP method.

In Sect. 2, we briefly review the formulation of the CIP method and give the computational details. The results and discussion for one-dimensional and double-slit systems are presented in Sect. 3. Conclusions are given in Sect. 4.

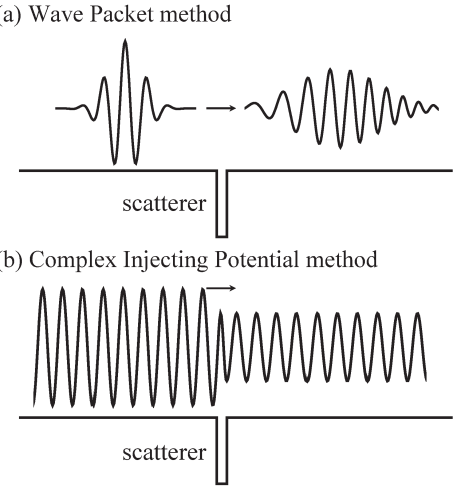

Fig. 1. Wave functions scattered by a square well potential of the (a) WP propagating method and (b) CIP method.

2. Method

2.1 Formalism

The TDSE is written as (Rydberg atomic units, $\hbar = 2m = e^2 = 1$, are used throughout the paper, unless stated otherwise):

$$\left(i\frac{\partial}{\partial t} - H_0\right)\psi(\mathbf{r}, t) = 0, \tag{1}$$

$$H_0 = -\nabla^2 + V(\mathbf{r}), \tag{2}$$

where H_0, $\psi(\mathbf{r}, t)$, and $V(\mathbf{r})$ are the Hamiltonian, wave function and external potential, respectively. The TDSE can be solved in an iterative manner numerically. In this study, we used the fourth-order Taylor expansion method for the time-evolution operator.[11)] Although the time-evolution operator in this method is not exactly unitary, the norm of the wave function is conserved with good accuracy by choosing a sufficiently small time step Δt.

We use the CIP method to inject electrons into a quantum system.[9)] The CIP method was formulated using a variational principle under the constraint of $\psi(\mathbf{r}_0, t) \equiv \phi(\mathbf{r}_0, t) = e^{-iEt}\hat{\phi}(\mathbf{r}_0)$. The variational functional is written as

$$S = \int dt \int d\mathbf{r}\, \psi(\mathbf{r},t)^* \left(i\frac{\partial}{\partial t} - H_0 \right) \psi(\mathbf{r},t) - \int dt \int d\mathbf{r}\, \lambda(\mathbf{r},t)[\delta(\mathbf{r}-\mathbf{r}_0)(\psi(\mathbf{r},t)^* - \phi(\mathbf{r},t)^*)] - \int dt \int d\mathbf{r}\, \lambda(\mathbf{r},t)^*[\delta(\mathbf{r}-\mathbf{r}_0)(\psi(\mathbf{r},t) - \phi(\mathbf{r},t))], \quad (3)$$

where $\lambda(\mathbf{r},t)$ is the Lagrange multiplier. By calculating $\delta S = 0$, the TDSE takes the form

$$\left(i\frac{\partial}{\partial t} - H \right) \psi(\mathbf{r},t) = 0, \quad (4)$$

$$H = H_0 + \frac{\lambda(\mathbf{r},t)\delta(\mathbf{r}-\mathbf{r}_0)}{\psi(\mathbf{r},t)}. \quad (5)$$

The Hamiltonian becomes time independent in the stationary and final state, and thus the Lagrange multiplier is chosen to be $\lambda(\mathbf{r},t) \sim e^{-iEt}$ to cancel the time dependence of the Hamiltonian for the stationary-state wave function $\psi(\mathbf{r},t) = e^{-iEt}\hat{\phi}(\mathbf{r})$. Accordingly, the modified Hamiltonian is given by

$$H = H_0 + ae^{-iEt}\frac{1}{\psi(\mathbf{r},t)}\delta(\mathbf{r}-\mathbf{r}_0), \quad (6)$$

where the second term is a *complex injecting potential*. In this method, we solve the modified TDSE, Eq. (4), with Eq. (6) at the source point $\mathbf{r}_0$, and solve the TDSE, Eq. (1), with Eq. (2). We can choose the constant a arbitrarily, because it only determines the amplitude of the wave function at the point $\mathbf{r}_0$.

2.2 *Computational details*

The simulations are carried out using a real-space grid. Thus, the wave function is represented on each grid point and the derivatives of the wave function are calculated by the fourth-order finite difference scheme. To avoid artificial reflections, a complex absorbing potential (CAP) is placed at the ends of the calculation box. The form of the CAP is the same as that suggested in Ref. 12. In a one-dimensional system the calculation box has a 80-Ry length with a grid spacing of 0.2 Ry and the width of the CAP is 20 Ry, while the calculation box is a square of $90 \times 90\,\mathrm{Ry}^2$ with a grid spacing of 0.3 Ry and the width of the CAP is 6.9 Ry in a two-dimensional system. We choose the initial wave function to be Gaussian at the source point $\mathbf{r}_0$ with a standard deviation of $\sigma = 5$ Ry. The simulations are carried out until $t = 2000$ Ry with a time step $\Delta t = 0.01$ Ry. The wave function and electron density are obtained at the end of the simulations when the stationary state has been reached.

The transmission coefficients are determined by the amplitudes of the incident wave and the transmitted wave, which are calculated from fitting the stationary-state wave function obtained from the simulations to the plane wave.[13)]

3. Results and Discussion

3.1 *Scattering in one dimension*

First, we consider electron scattering by a rectangular potential barrier in one dimension,

$$V(x) = \begin{cases} V_0 & \text{for } 0 < x < d \\ 0 & \text{otherwise} \end{cases}, \quad (7)$$

where $V_0 = 4$ Ry and $d = 2$ Ry are chosen. The incident-energy dependent transmission coefficients are calculated and shown in Fig. 2. The blue solid curve indicates the analytical solution, while the black dots indicate the calculated values. The calculated values are in good agreement with the analytical solution. To check the validity of the present method, we also simulated electron scattering by a unique potential,[14,15)]

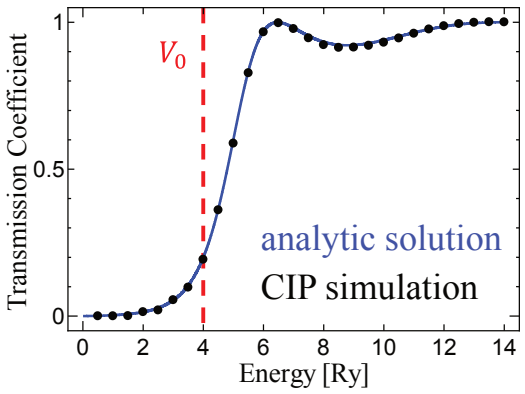

Fig. 2. (Color online) Energy dependence of the transmission coefficient for a rectangular potential barrier. The blue line indicates the analytical solution, while the black dots indicate the calculated values.

$$V(x) = -\alpha^2 n(n+1)\,\mathrm{sech}^2(\alpha x), \quad (8)$$

for which the transmission coefficient is exactly one at any incident energy, when n is a positive integer. In our simulation, the parameters are chosen to be $n = 1$ and $\alpha = 1$, and the incident energy is $E = 2$ Ry. The calculated transmission coefficient is $T = 1.00001$, so the numerical accuracy in the coefficient is 10^{-5}, indicating that the present method is reliable for practical use.

3.2 *Scattering by a double slit*

Here, we calculate the interference patterns of scattered-electron intensity (IPSEI) by a double-slit barrier. A double-slit Gedankenexperiment for electrons that demonstrates the wave–particle duality of electrons was first introduced by Feynman.[16)] Feynman remarked that the experiment would be difficult to conduct because the apparatus would have to be made on an extremely small scale. However, a double-slit experiment for electrons were carried out by Jönsson in 1961[17,18)] and Merli et al. in 1976.[19)] Later, Tonomura et al. performed a double-slit experiment in 1989,[20)] which was selected as one of the most beautiful experiments by *Physics World*.[21)] In the numerical simulation of electron scattering by a double slit using the WP method for solving the TDSE, the IPSEI has been calculated.[1)] Recently, an extremely interesting result on IPSEI through asymmetric double-slit experiments was reported, where the electrons were categorized into three groups: electrons that passed through only the first slit, electrons passing through only the other slit, and electrons passing through both slits simultaneously.[22)]

Figure 3 shows the calculation box used in the present simulations. The black rectangles denote the wall, with $d = 2.4$ Ry and $W = 5$ Ry. The CIP is placed at the red point, which is 15 Ry away from the center wall. The IPSEI are observed at the black half circle of $H = 36$ Ry. The incident energy is $E = 50$ eV, which corresponds to a wavelength of $\lambda = 3.3$ Ry.

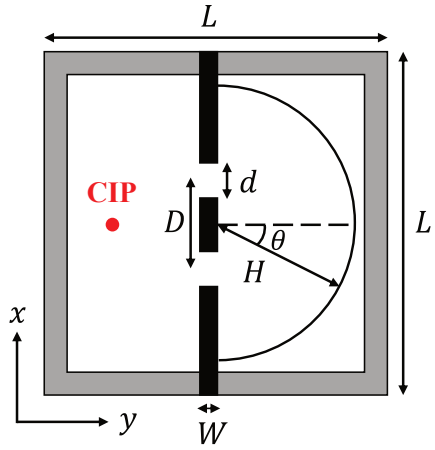

Fig. 3. (Color online) Schematic diagram of the calculation box. $L = 90$ Ry for each side of the square box. The black rectangles denote a wall of thickness $W = 5$ Ry with slits of width $d = 2.4$ Ry. Interference patterns of the scattered-electron intensity are observed at the black half circle of $H = 36$ Ry. The CIP is placed 15 Ry away from the wall. The CAP is placed at the box boundaries, shown by the gray area.

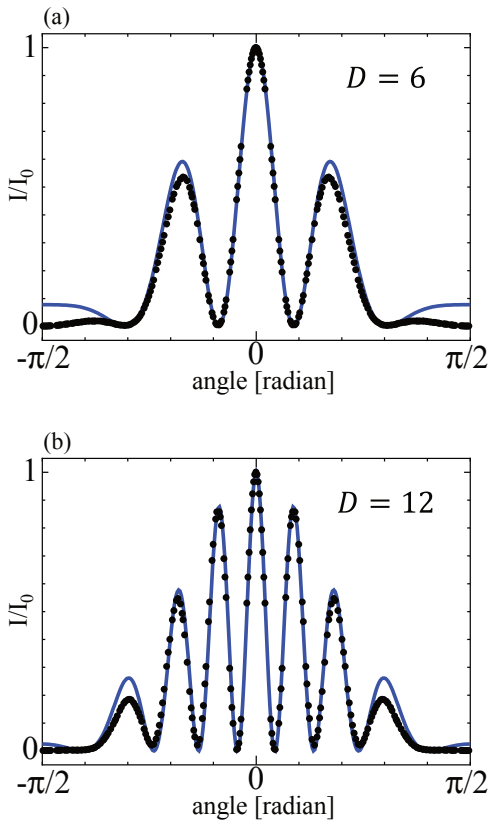

Fig. 4. (Color online) IPSEI for two double-slits of different gaps D: (a) $D = 6$ Ry and (b) $D = 12$ Ry. The black dots indicate the results of our simulation, while the blue solid curves indicate the analytic values calculated by Eq. (9).

The IPSEI for the two double-slits of different gaps D are shown in Fig. 4. The black dots indicate the results of the simulations, while the blue solid curves indicate the analytic form obtained in the optics:[23)]

$$I(s) = I_0 \frac{\sin^2(kds/2)}{(kds/2)^2} \cos^2\left(\frac{kDs}{2}\right), \quad s = \sin\theta, \tag{9}$$

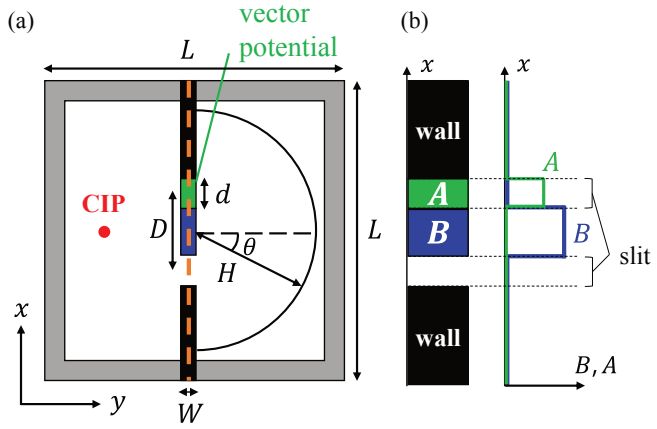

Fig. 5. (Color online) (a) Schematic diagram of the calculation box. The shape and dimensions of the box and the double slit are the same as in Fig. 3. A magnetic flux exists in the center wall (blue-colored) and the vector potential exists only inside the upper slit (green-colored). (b) Schematic (left) and field distributions (right) of the magnetic field and vector potential along the orange dashed line in (a).

where k, d, and θ are the wave number, slit width and angle defined in Fig. 3, respectively. The simulated results reproduce the overall features and D dependence of IPSEI fairly well. We note that the differences in bigger angle in Figs. 4(a) and 4(b) are caused by the different conditions on between the derivation of Eq. (9) and our simulation. In the derivation of the optical formula of Eq. (9), light is diffracted by the double slits with zero thickness. In our simulation, however, the electrons are diffracted by the double slits with finite thickness in which reflections appear. As a result, the IPSEI are influenced by the slit thickness as discussed by Endoh et al. in Ref. 24. We actually find the agreement of IPSEI in bigger angle between the calculated values and analytical ones in a single-slit configuration by using zero thickness slit in our simulation. This is not shown in our paper.

3.3 Aharonov–Bohm effect

We numerically demonstrate the Aharonov–Bohm (AB) effect, which was theoretically introduced by Aharonov and Bohm in 1959[25)] and first experimentally observed by Tonomura et al. in 1986.[26)] The AB effect dictates that a physical quantity experienced by electrons is not an electromagnetic field but is a vector potential. Since the vector potential modifies the phase of an electron's wave function, the IPSEI by an *asymmetric* double slit caused by a vector potential is strongly influenced. Figure 5 shows the distributions of the vector potential and the corresponding magnetic field in the double slit used in the simulation. The size of the system and the incident energy are the same as for the above simulations with $D = 12$ Ry.

We consider a situation for which the magnetic flux Φ exists only inside the center wall (blue-colored). A uniform magnetic field $\mathbf{B}$ is determined to satisfy the relation $\Phi = \int \mathbf{B} \cdot d\mathbf{S}$, and the vector potential $\mathbf{A}$ is similarly determined to satisfy the relation $\mathbf{B} = \nabla \times \mathbf{A}$. The vector potential in the Landau gauge is[1)]

$$\mathbf{A}(x, y) = (0, A_y(x), 0), \tag{10}$$

where

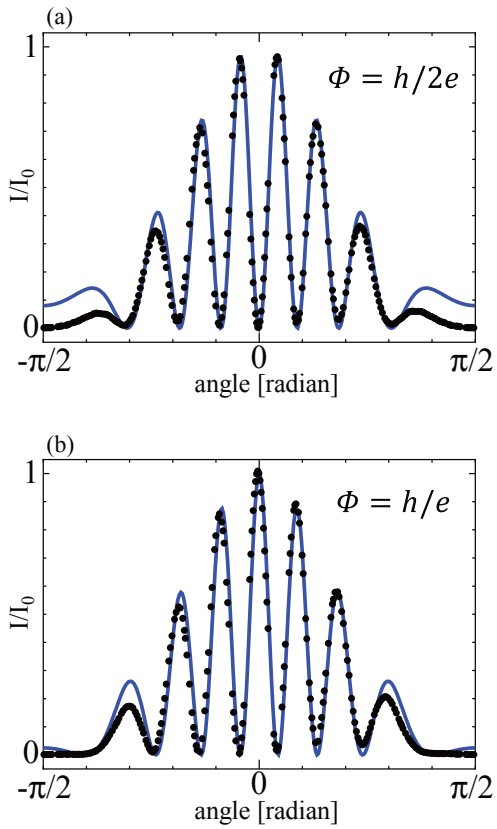

Fig. 6. (Color online) IPSEI for different magnetic fluxes Φ: (a) $\Phi = h/2e$ and (b) $\Phi = h/e$. The black dots indicate the results of our simulation, while the blue solid curve indicates the analytic values calculated from Eq. (13).

$$A_y(x) = \begin{cases} B(D-d) & : \text{inside the upper slit} \\ 0 & : \text{in the other area} \end{cases}. \qquad (11)$$

Based on this, the magnetic field exists only in the center wall (blue-colored) and the vector potential exists only inside the upper slit (green-colored). We use the minimal-coupling Hamiltonian given by

$$H_0 = -\frac{\hbar^2}{2m}\left(\nabla + \frac{ie}{\hbar}\mathbf{A}\right)^2 + V(\mathbf{r}), \qquad (12)$$

instead of Eq. (2). Here, e is the absolute value of the electron's charge. In this subsection, we use SI units.

The IPSEI for different magnetic fluxes are shown in Fig. 6. The black dots indicate the results of the simulations, while the blue solid curves indicate the analytic form:

$$I(s) = I_0 \frac{\sin^2(kds/2)}{(kds/2)^2}\cos^2(\Delta\phi), \quad s = \sin\theta. \qquad (13)$$

Here, $\Delta\phi$ is the phase difference of electrons from the two slits, which is defined as

$$\Delta\phi = \frac{kDs}{2} - \frac{e\Phi}{2\hbar}. \qquad (14)$$

The IPSEI agree with the analytical values, as clearly shown in Figs. 6(a) and 6(b). The AB phase shift is π in Fig. 6(a) and 2π in Fig. 6(b). Figure 6 indicates that the interaction of electrons with the vector potential is correctly taken into account by the stationary electron-wave method. It is noted that the calculated values (black dots) are asymmetry. The asymmetry is considered to originate from the numerical errors that is caused by the asymmetric vector-potential distribution in the double-slit configuration [Fig. 5(b)]. The differences in IPSEI between the calculated values and analytical ones in bigger angle in Figs. 6(a) and 6(b) are due to the same reason as that discussed in Figs. 4(a) and 4(b).

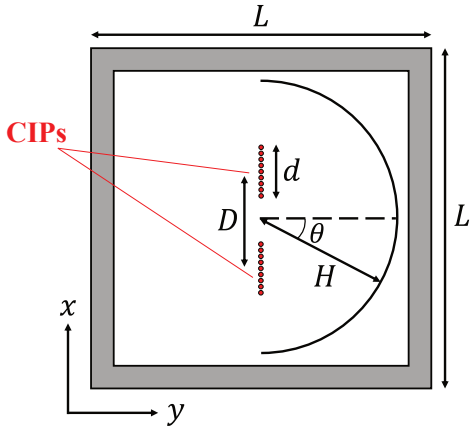

Fig. 7. (Color online) Schematic diagram of the calculation box. The shape and dimensions of the box are the same as in Fig. 3. The CIPs are arranged in a line, illustrated as red points, instead of two slits.

3.4 Arranged CIPs for double sources

Lastly, we construct a new form of a double source using multiple CIPs, as shown in Fig. 7 as an alternative to the conventional type shown in Figs. 3 and 4. We calculate the IPSEI generated by the double multiple-CIP sources. In this set up, the center wall is removed and nine CIPs are uniformly arranged at intervals of 0.3 Ry on each side, corresponding to a slit width of $d = 2.4$ Ry. The IPSEI for the two double sources with different D are shown in Fig. 8. The red solid curves indicate the results for the arranged-CIP method, while the black solid curves are the same as the black dots in Fig. 4. The agreement of the IPSEI between the apparently different configurations of Figs. 3 and 7 indicates that the electron wave function passing through the double slits can be interpreted as that launched from individual point sources (CIP here) within each slit, which follows Huygens's principle.

It is of interest to note that the present configuration (double sources with multiple CIPs) is similar to that of an experiment observing the interference patterns of Bose–Einstein condensates (BECs).[27,28] In this experiment,[27] two separate BECs were first trapped by a double-well potential. The two BECs expanded immediately after the potential was switched off and the interference pattern generated by the two BECs was observed. The overall features of the interference patterns in Fig. 2 of Ref. 27 are similar to those of Fig. 8 of this paper. Since the initial phases of the two BECs are not necessarily the same and the interference pattern was changed by the phase difference, it is useful to simulate beforehand the phase-difference dependent interference pattern of the BECs. We can simulate the situation easily by introducing a phase shift in the Hamiltonian,

$$H = H_0 + ae^{-iEt}\sum_{i=1}^{9}\frac{\delta(\mathbf{r}-\mathbf{r}_i)}{\psi(\mathbf{r},t)} + ae^{-i(Et-\gamma)}\sum_{j=1}^{9}\frac{\delta(\mathbf{r}-\mathbf{r}_j)}{\psi(\mathbf{r},t)}, \qquad (15)$$

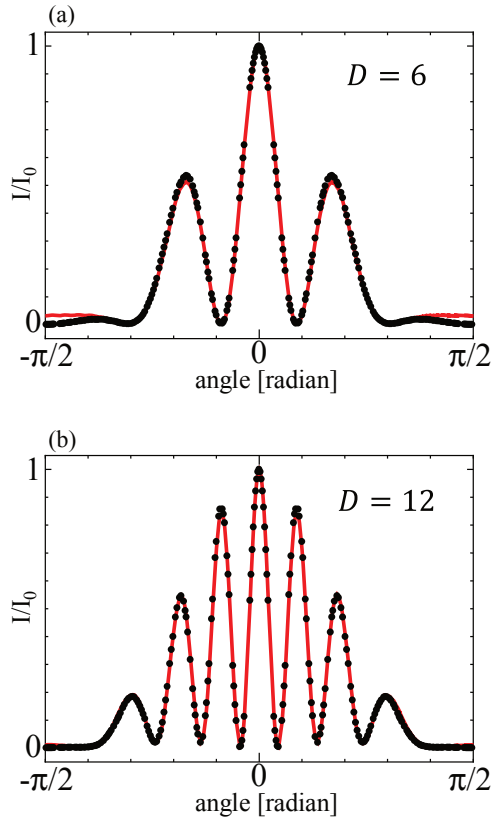

Fig. 8. (Color online) IPSEI for different distances between the two line CIP sources. The red solid curves indicate the results for the arranged CIPs method, while the black curves are the same as the black dots in Fig. 4.

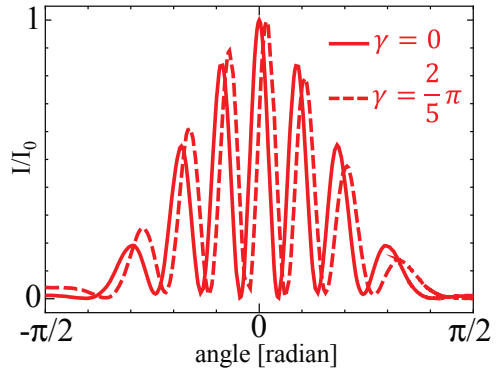

Fig. 9. (Color online) The red solid curve indicates the result for $\gamma = 0$, which is the same as the red solid curve in Fig. 8(b), while the red dashed curve indicates the result for $\gamma = \frac{2}{5}\pi$.

where γ, $\mathbf{r}_i$, and $\mathbf{r}_j$ are the phase shift and the position of the CIPs inside the lower slit and the upper slit, respectively. The red solid curve indicates the result for $\gamma = 0$, which is the same as the red solid curve in Fig. 8(b), while the red dashed curve indicates the result for $\gamma = \frac{2}{5}\pi$. The (fractional) phase shift effect on the interference patterns is clearly demonstrated by Eq. (15), as seen in Fig. 9. Therefore, the present technique, which enables control of the phase difference between two independent sources, also contributes toward explaining the detailed interference patterns of BECs observed in experiments.

4. Conclusion

We simulated stationary-state electron scattering in one dimension and in a double-slit system by solving the TDSE with a CIP. The transmission coefficients through one-dimensional potentials and the IPSEI caused by double slits show good agreement with analytical results. The interaction between electrons and the vector potential is properly taken into account in the AB effect simulation. Also, from the simulation of the arranged-CIP method, we predict that this new method can be applied to BEC interference simulations.

Since the present method can be straightforwardly extended to TDDFT, we can simulate field electron emission, photo-induced electron emission, secondary electron emission, thermionic emission, and so on.

Acknowledgment The authors wish to thank Y. Suzuki for discussions on CIP, T. Yamamoto for suggestion on the AB effect and S. Watabe for valuable discussions regarding BEC interference. The work of K.W. was supported by JPSJ KAKENHI (Grant No. JP16K05483). The numerical calculations were performed on supercomputers at the Institute for Solid State Physics, University of Tokyo, Japan.

*kwatanabe@rs.tus.ac.jp

1) N. Watanabe and M. Tsukada, J. Phys. Soc. Jpn. **69**, 2962 (2000).
2) Y. Ueda, Y. Suzuki, and K. Watanabe, Phys. Rev. B **94**, 035403 (2016).
3) Y. Ueda, Y. Suzuki, and K. Watanabe, Appl. Phys. Express **11**, 105101 (2018).
4) Y. Ueda, Y. Suzuki, and K. Watanabe, Phys. Rev. B **97**, 075406 (2018).
5) H. Miyauchi, Y. Ueda, Y. Suzuki, and K. Watanabe, Phys. Rev. B **95**, 125425 (2017).
6) J.-A. Yan, J. A. Driscoll, B. K. Wyatt, K. Varga, and S. T. Pantelides, Phys. Rev. B **84**, 224117 (2011).
7) K. Tsubonoya, C. Hu, and K. Watanabe, Phys. Rev. B **90**, 035416 (2014).
8) J. A. Salas, K. Varga, J.-A. Yan, and K. H. Bevan, Phys. Rev. B **93**, 104305 (2016).
9) D. B. Wibking and K. Varga, Phys. Lett. A **376**, 365 (2012).
10) S. He, C. Covington, and K. Varga, J. Appl. Phys. **123**, 165102 (2018).
11) K. Yabana and G. F. Bertsch, Phys. Rev. B **54**, 4484 (1996).
12) T. Gonzalez-Lezana, E. J. Rackham, and D. E. Manolopoulos, J. Chem. Phys. **120**, 2247 (2004).
13) K. Varga and J. A. Driscoll, *Computational Nanoscience* (Cambridge University Press, Cambridge, U.K., 2011) p. 147.
14) L. D. Landau and E. M. Lifshitz, *Quantum Mechanics: Non-relativistic Theory* (Pergamon Press, London, 1977) Vol. 3, 3rd ed., p. 80.
15) S. Flügge, *Practical Quantum Mechanics I* (Springer, Berlin, 1971) p. 94.
16) R. P. Feynman, R. B. Leighton, and M. Sands, *The Feynman Lectures on Physics* (Addison-Wesley, Reading, MA, 1965) Vol. 3, Chap. 1.
17) C. Jönsson, Z. Phys. **161**, 454 (1961).
18) C. Jönsson, Am. J. Phys. **42**, 4 (1974).
19) P. G. Merli, G. F. Missiroli, and G. Pozzi, Am. J. Phys. **44**, 306 (1976).
20) A. Tonomura, J. Endo, T. Matsuda, T. Kawasaki, and H. Ezawa, Am. J. Phys. **57**, 117 (1989).
21) R. P. Crease, Phys. World **15**, 17 (2002).
22) K. Harada, T. Akashi, K. Niitsu, K. Shimada, Y. Ono, D. Shindo, H. Shinada, and S. Mori, Sci. Rep. **8**, 1008 (2018).
23) E. Hecht, *Optics* (Addison-Wesley, Reading, MA, 2002) 4th ed., p. 385.
24) A. Endoh, S. Sasa, H. Arimoto, and S. Muto, J. Appl. Phys. **86**, 6249 (1999).
25) Y. Aharonov and D. Bohm, Phys. Rev. **115**, 485 (1959).
26) A. Tonomura, N. Osakabe, T. Matsuda, T. Kawasaki, J. Endo, S. Yano, and H. Yamada, Phys. Rev. Lett. **56**, 792 (1986).
27) M. R. Andrews, C. G. Townsend, H.-J. Miesner, D. S. Durfee, D. M. Kurn, and W. Ketterle, Science **275**, 637 (1997).
28) M. Greiner, O. Mandel, T. Esslinger, T. W. Hänsch, and I. Bloch, Nature **415**, 39 (2002).